Asymmetric Flux Barrier and Skew Design Optimization of Reluctance Synchronous Machines

Eduan Howard, *Student Member, IEEE*, Maarten J. Kamper, *Senior Member, IEEE*, and Stiaan Gerber, *Student Member, IEEE*

***Abstract*—In this paper, an investigation into an alternative topology for reluctance synchronous machine rotor flux barriers is presented. The investigated topology employs a high number of flux barrier variables with an alternative asymmetric rotor structure. The focus in this paper is on maximizing average torque and minimizing torque ripple, using finite element-based design optimization, in order to study the possibility of achieving acceptably low torque ripple. A subsequent investigation into the effect of rotor skew on the proposed optimized design to reduce torque ripple even further is also conducted, as well as the manufacturing and testing of the proposed flux barrier prototype.**

***Index Terms*—AC motors, asymmetric flux barrier, asymmetric pole structure, finite-element analysis, optimization algorithms, rotor skew, synchronous reluctance machine.**

I. Introduction

With the increasing emphasis on efficiency and cost reduction, the interest in reluctance synchronous machines (RSMs) has grown during the past decade. This interest is driven not only by the robustness, efficiency, and simplicity of RSMs but also by the fact that the cost of rare-earth magnets is increasing and their market stability is decreasing.

The main focus of most RSM design optimization, depending on application, is on maximizing average torque (T_A), within the limits of an allowable volume, and minimizing torque ripple (T_R). The latter is conventionally achieved by rotor skewing and stator cording in order to reduce the airgap harmonics that produce a high T_R. In this paper, the possibility of both maximizing T_A and minimizing T_R without implementing rotor skew techniques to achieve acceptable T_R values is investigated. A further investigation into the effect of rotor skew on the proposed topology to reduce T_R values even further is also presented.

A large part of the design of RSMs is focused on the rotor creation and, more specifically, the type of flux barrier topology and its creation procedure. With the latter in mind, two creation techniques are summarized by Vagati *et al.* [1], the first of which implements the generalized lumped-parameter modeling of the rotor magnetic circuit and the second is a numeric design optimization of a rotor flux barrier structure.


(a) (b) (c)

Fig. 1. Rotor flux barrier profiles of four-pole RSMs in the literature.

The second procedure is implemented in this research. This procedure is based on a predetermined basic barrier structure with a fixed number of variable parameters, such as barrier tip angle and barrier width. These parameters are numerically optimized by implementing a finite element (FE) method package that calculates each iteration's relevant machine performance parameters, for example, torque and torque ripple. Examples of this design procedure can be found in [2]–[5]. The advantage of this approach is that the optimization inherently takes complex phenomena, such as torque harmonics and cross saturation, into account.

In RSM design, three basic rotor topologies have emerged with combinations and small variations between specific research projects. These three shapes are illustrated in Fig. 1.

The first of these topologies, shown in Fig. 1(a), is created by implementing straight lines to create the flux barriers. Examples of these are presented in [3] and [6]. The second topology, (b), is created by implementing circles to generate the respective flux barriers with examples provided in [2], [7], and [8]. The third topology, (c), implements second-order polynomials, as illustrated in [9].

In all of the above, the basic shape of the flux barriers is predetermined. The question may then arise as to what barrier shape would emerge if an optimizer is given more freedom to shape the barrier. In this paper, a combined topology that integrates both topology types (a) and (c) in Fig. 1 is presented. This allows a much wider variation in the shape of the flux barriers within the rotor design parameters. The proposed topology can conform to either topology (a) or (c), or a combination of the two.

An additional topological feature that has been investigated in the literature is the barrier tip, with authors implementing a variety of shapes. An ideal shape is yet to emerge. In this paper,

Manuscript received October 29, 2014; revised February 11, 2015; accepted April 2, 2015. Date of publication May 5, 2015; date of current version September 16, 2015. Paper 2014-EMC-0667.R1, presented at the 2014 International Conference on Electrical Machines, Berlin, Germany, September 2–5, and approved for publication in the IEEE Transactions on Industry Applications by the Electric Machines Committee of the IEEE Industry Applications Society. This work was supported by ABB Corporate Research, Sweden.

The authors are with the Department of Electrical and Electronic Engineering, Stellenbosch University, Stellenbosch 7602, South Africa (e-mail: eduanhoward@telkomsa.net; kamper@sun.ac.za; sgerber@sun.ac.za).

Color versions of one or more of the figures in this paper are available online at http://ieeexplore.ieee.org.

Digital Object Identifier 10.1109/TIA.2015.2429649

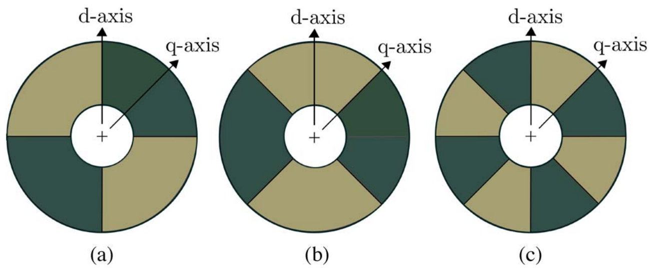

Fig. 2. Four-pole asymmetric structure illustrating the different pole topologies with (a) asymmetric rotor structures about the d-axis with symmetric q-axis, (b) asymmetric rotor structures about the q-axis with symmetric d-axis, and (c) asymmetric rotor structures about the q- and d-axes.

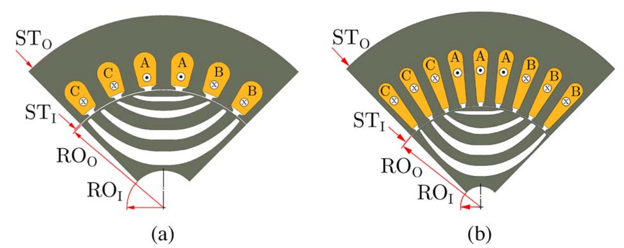

Fig. 3. (a) 24-slot RSM with specifications in Table I, $RO_O = 39.7$ mm, $RO_I = 12.5$ mm, a stack length of 122 mm, and an air-gap length of 0.3 mm. (b) 36-slot RSM with specifications in Table I, $RO_O = 52.2$ mm, $RO_I = 21.5$ mm, a stack length of 133.5 mm, and an air-gap length of 0.35 mm.

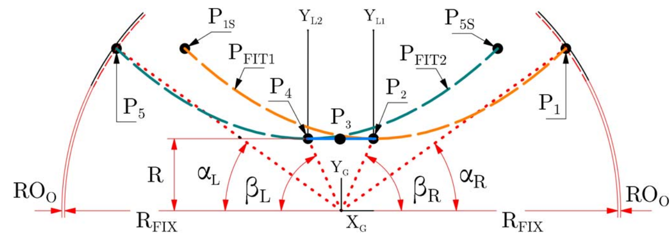

Fig. 4. Flux barrier creation variables with subscript G, the global axis, and L, the two local axes.

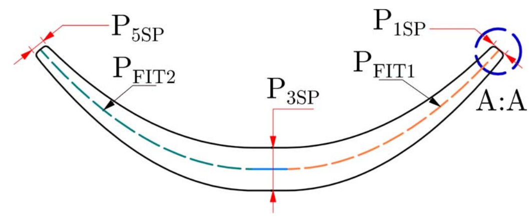

Fig. 5. Flux barrier point width variables.

the barrier tips are generated using cubic splines. This gives the optimizer the ability to produce a variety of barrier tip shapes during optimization.

To further increase the freedom of the optimizing algorithm, an asymmetric pole structure (ASPS) is proposed. A common approach to implement an ASPS is illustrated in Fig. 2(a), where the rotor topology is asymmetric about the d-axes but symmetric about the q-axes. Examples of this RSM design are illustrated in studies [10]–[13]. An alternative asymmetric rotor is illustrated in Fig. 2(b), where the topology is symmetric about the d-axes and asymmetric about the q-axes. In this paper, an ASPS, as illustrated in Fig. 2(c), is implemented, in which the d-axes and q-axes are lines of asymmetry. This results in a rotor with four identical poles and allows a quarter section of the machine to be modeled, compared to the half sections required in the case of Fig. 2(a) or (b).

The topology proposed in this paper may have a variation in machine performance, depending on the direction of rotation and mode of operation (motor or generator). For this paper, a unidirectional machine application is assumed, with possible industrial applications, including pumps, fans, and conveyor drives.

This paper consists of six sections. In Section II, the parameters of the suggested topology are described in detail. In Section III, the optimization process and strategies that were implemented, along with an illustration of the results that were achieved, are discussed. The effect of rotor skew on the optimized asymmetric rotor topology is investigated in Section IV. For the purpose of validation, experimental results achieved with a selected rotor are presented in Section V. Finally, the findings of this paper are summarized in Section VI.

II. Topology Creation

For the suggested model, two existing stators were selected to investigate the newly suggested rotor flux barrier topology. The first is an existing 24-slot induction machine stator, and the second is an existing 36-slot stator from an RSM machine optimized for topology (b) in Fig. 1 by Kamper et al. [2]. The selected stators, along with the rotor topologies, are illustrated in Fig. 3. As can be seen in the figure, the central support web commonly implemented [2], [7], [8], [14], [15] in the barrier creation for rotor rigidity has been omitted. This omission is in order to increase the saliency ratio and, hence, the performance of the machine, as suggested in [9].

A. Barrier Construction

An illustration of the new proposed flux barrier topology is shown in Figs. 4 and 5. The main parameters of the topology are points P_1 to P_5 with symmetric points P_{1S} and P_{5S} created around the respective local y-axes, Y_{L1} and Y_{L2}. These points are then -order polynomial fittings to create the barrier "midline." The fittings consist of P_{FIT1} through points P_1, P_2, and P_{1S} and P_{FIT2} through points P_{5S}, P_4, and P_5. Finally, a horizontal line, connecting the respective polynomial vertex points P_2 and P_4, concludes the barrier "midline" construction. The width of the barrier is defined by P_{1SP}, P_{3SP}, and P_{5SP}, as shown in Fig. 5, with the fitting procedure for the midline repeated for both the top and bottom barrier lines.

The curve fitting consists of a second-order polynomial

$$p(x) = c_0 + c_1 \cdot x + c_2 \cdot x^2 \tag{1}$$

with the coefficient matrix of the coefficients p in the Vandermond matrix format [16] with the solution square error of the fitting minimized by

$$E = \sum_{k}^{j=0} |p(x_j) - y_j|^2 \,. \tag{2}$$

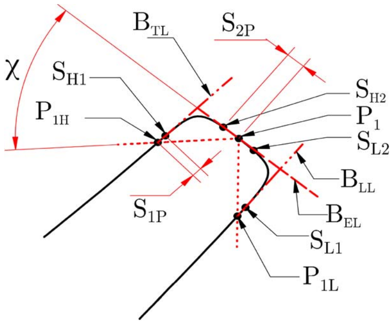

Fig. 6. Bezier cubic spline fitting of section **A:A** in Fig. 5.

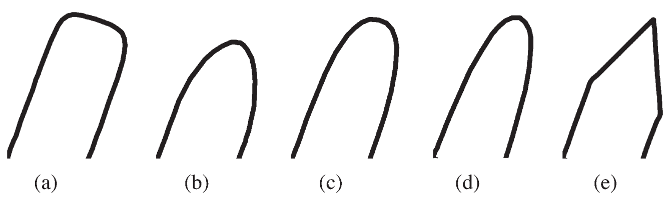

Fig. 7. Five examples of the possible flux barrier tip shapes, with a multitude of in-between variations that could be achieved with the variables in Fig. 6.

Coordinates of points P_1 and P_5 consist of a constant preset radius R_{FIX} and an angle α, as indicated in Fig. 4. The coordinates of the y-axis vertex point of the two fitted polynomials consist of a vertical displacement R and a lateral displacement angle β specifying the displacement to vertex points P_2 and P_4, respectively. Concluding the barrier construction, five variables (namely, α_R, β_L, R, P_{3sp}, and P_{1sp}) are used to create one barrier for the symmetric case, with the addition of three variables (α_L, β_L, and P_{5sp}) for the asymmetric case.

B. Barrier Tip Construction

Due to the extreme sensitivity of T_R in RSMs as the low percentage T_R values are approached, as presented in [12], the end tip shapes of the barriers are additionally adjusted with the addition of more variability for the optimization algorithm to utilize. Fig. 6 is an illustration of one barrier tip with its location in section **A:A** in Fig. 5. In this figure, the original barrier lines are visible and annotated by the barrier top limit (B_{TL}), the barrier lower limit(B_{LL}), and the barrier end limit(B_{EL}).

In order to reduce the sharp force concentrating areas at the tips of the barriers and to give the optimizer more variability in the most sensitive T_R area, a Bezier cubic spline fitting is utilized. This spline fitting consists of four points: a start point, P_{1_H} or P_{1_L}; a stopping point P_1; and two points indicating the departure angles from the start point to the end point, points S_{H1} and S_{H2} or points S_{L1} and S_{L2}. The locations of P_{1_H} and P_{1_L} on the B_{TL} and B_{LL} lines are determined by the angle χ. Fig. 7 illustrates five examples of flux barrier tips that could be achieved by the optimizer, with a multitude of variations possible between Fig. 7(a) and (e).

With these added variables, each symmetric barrier now consists of eight variables (namely, α_R, β_R, R, P_{3sp}, P_{1sp}, χ, S_{1P}, and S_{2P}). Each variable consists of a matrix containing each respective barrier's correlating variable, as illustrated in

TABLE I
STATOR SPECIFICATIONS OF THE 24-SLOT AND 36-SLOT MACHINES (N_{ST}—THE NUMBER OF SERIES TURNS PER PHASE)

	Stator Rated Machine Specifications						
Stator	V $[V]$	I $[A]$	f_e $[Hz]$	ST_I $[m]$	ST_O $[m]$	N_{ST}	J $[A/mm^2]$
24-Slot	400	3.5	50	0.08	0.13	132	±6.4
36-Slot	150	42	50	0.1051	0.2032	36	±6.4

(3) for the symmetric barrier case, with n being the number of barriers implemented. Four barriers are chosen for the final design in order to reduce T_R as much as possible, as illustrated in [11], where an increase in barriers indicates a decrease in T_R

$$\begin{bmatrix} \alpha_R \\ \beta_R \\ R \\ P_{3sp} \\ P_{1sp} \\ \chi \\ S_{1P} \\ S_{2P} \end{bmatrix} = \begin{bmatrix} \alpha_{(R)1} & \cdot & \cdot & \alpha_{(R)n} \\ \beta_{(R)1} & \cdot & \cdot & \beta_{(R)n} \\ R_1 & \cdot & \cdot & R_n \\ P_{(3sp)1} & \cdot & \cdot & P_{(3sp)n} \\ P_{(1sp)1} & \cdot & \cdot & P_{(1sp)n} \\ \chi_1 & \cdot & \cdot & \chi_n \\ S_{(1P)1} & \cdot & \cdot & S_{(1P)n} \\ S_{(2P)1} & \cdot & \cdot & S_{(2P)n} \end{bmatrix}. \quad (3)$$

III. Optimization

A. Motor Parameter Calculation

For the motor parameter FE simulation, the rated current density conditions for the respective stators are used as tabulated in Table I. In an attempt to reduce the design optimization time, an alternative FE simulation package is used, namely, SEMFEM, that was developed in-house by Gerber [17]. The advantage of this package is its greatly reduced FE simulation solving time as compared to commercial FE simulation packages. This is as a result of its script-based interface.

Each FE simulation is set up with the rotor rotating an equivalent electrical angle of 60°. This equates to a two-slot pitch angle for the 24-slot stator and a three-slot pitch angle for the 36-slot stator. The number of time steps for each simulation is set to 50. The machine performance parameter T_R is calculated by

$$T_R = \frac{T_{(MAX)} - T_{(MIN)}}{T_A} \quad (4)$$

with T_{MAX} and T_{MIN} being the maximum and minimum torque values of the simulated machine, respectively, and T_A being the average simulation torque.

B. Optimization Procedure

For the optimization, the VisualDoc [18] software package was used. The flow diagram of the optimization procedure is illustrated in Fig. 8. The simulation time for the 24-slot machine, which includes the reading in of variables, reconstructing the updated topology, setting up the FE package, solving, and postprocessing, was approximately 30 s. The same procedure for the 36-slot machine was concluded in 95 s.

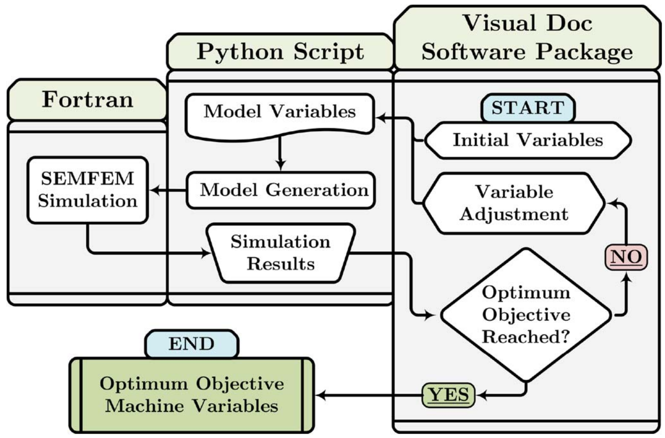

Fig. 8. Optimization flow diagram implementing a Python script to link the optimization package VisualDoc with the FE package SEMFEM for design optimization.

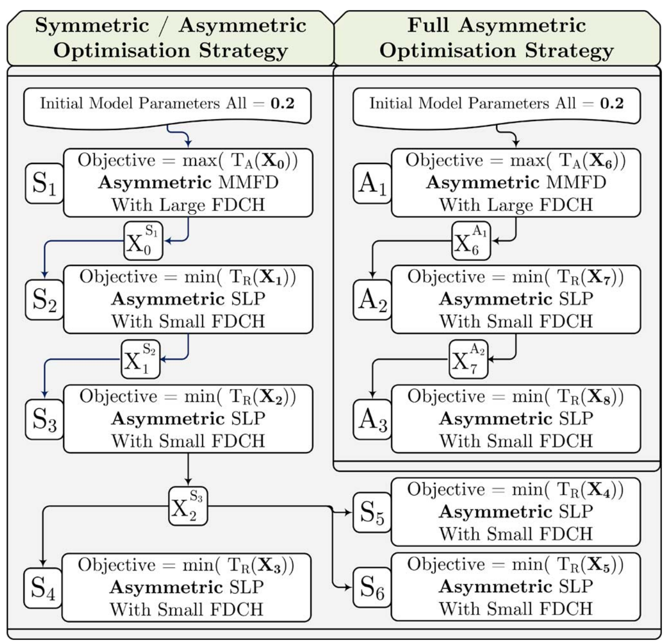

Fig. 9. Optimization strategies implemented and variable flow diagram, with the superscript "S" indicating the implementation of the symmetric–asymmetric procedure and superscript "A" indicating that of the full-asymmetric optimization procedure.

The optimization of the rotor topology consists of two separate strategies, as presented in Fig. 9, with the initial strategy being a symmetric–asymmetric strategy (SAS) and the second being a full-asymmetric strategy (FAS). The optimization objectives of both strategies are to maximize T_A and minimize T_R. The initial global search for maximizing T_A is conducted by a relatively large finite difference step size, followed by an unconstrained minimization of T_R with a small finite difference step size (FDCH).

The objective T_A is maximized by using a gradient-based optimization algorithm, namely, the modified method of feasible directions (MMFD) [19]; objective T_R is minimized by utilizing the optimization algorithm sequential linear programming [19]. These specific algorithms were selected based on the consistency with which an optimum solution could be determined for each respective optimization problem.

TABLE II
OPTIMIZATION VARIABLES*

	SAS Optimisation						**FAS** Optimisation		
	X_0	X_1	X_2	X_3	X_4	X_5	X_6	X_7	X_8
α	$\surd_R$	$\surd_R$	$\surd_R$	$\surd_L$	$\surd$	$\surd$	$\surd$	$\surd$	$\surd$
β	$\surd_R$		$\surd_R$		$\surd$	$\surd$	$\surd$		$\surd$
R	$\surd$		$\surd$		$\surd$	$\surd$	$\surd$		$\surd$
P_{1sp}	$\surd$		$\surd$		$\surd$	$\surd$	$\surd$		$\surd$
P_{3sp}	$\surd$		$\surd$		$\surd$	$\surd$	$\surd$		$\surd$
P_{5sp}					$\surd$	$\surd$	$\surd$		$\surd$
χ	$\surd_R$		$\surd_R$		$\surd$	$\surd$	$\surd$		$\surd$
S_1P	$\surd_R$		$\surd_R$		$\surd$	$\surd$			
S_2P	$\surd_R$		$\surd_R$		$\surd$	$\surd$			
θ	$\surd$			$\surd$		$\surd$	$\surd$		

* $\surd_R$ - Right Side, $\surd_L$ - Left Side, $\surd$ - Right & Left Sides
Referring to the right and left sides of the asymmetric pole structure.

1) Symmetric–Asymmetric Optimization Strategy: For the initial study on the 24-slot and 36-slot motors, the flux barrier topologies are first symmetrically optimized by maximizing $T_A(X_0)$, with the R subscript of variables X_O in Table II indicating the right symmetric barrier side. This is done in order to speed up the optimization procedure by reducing the number of variables and also to provide a baseline for comparative optimized asymmetric structures.

For the symmetric optimization, points P_{5SP}, α_L, and β_L are symmetrically generated around the global y-axis from points P_{1SP}, α_R, and β_R, with the barrier tips symmetrically reproduced for each respective barrier. All variables, including the rated current density conditions on the stator, are kept constant, excluding the current angle θ, which is allowed to vary between 45° and 90°. Furthermore, the inside and outside rotor radii were fixed during optimization.

After the symmetric maximization, the second objective function is symmetrically minimized, using solution variables $X_0^{S_1}$ as start variables. The minimization is performed in two steps, first by constraining all the variables except those summarized by X_1 in Table II, with objective function $T_R(X_1)$, and second with all the variables allowed to vary symmetrically with the objective function, $T_R(X_2)$. The latter is conducted with the current angle θ constrained by implementing the variables $X_1^{S_2}$ as start variables. The optimization result of S_3 in Fig. 9 is now implemented in three separate optimization studies (S_4, S_5, and S_6), using the 24-slot machine to determine the effects of the proposed asymmetric topology on the symmetric machine performance results.

The design optimization study S_4 consists of the minimization of objective function $T_R(X_3)$, with variables X_3 in Table II and with only the current angle and asymmetric left side allowed to vary. The second and third optimizations (S_5 and S_6) consist of minimizing optimization objective functions $T_R(X_4)$ and $T_R(X_5)$. The variables of X_4 equal those of X_5, with the addition of the current angle θ that is also allowed to vary in X_5.

The performance results of the four optimization objectives are illustrated in Fig. 10, in which the four different topologies found are mapped against the current angle change for the 24-slot machine. The tabulated values for each of the four

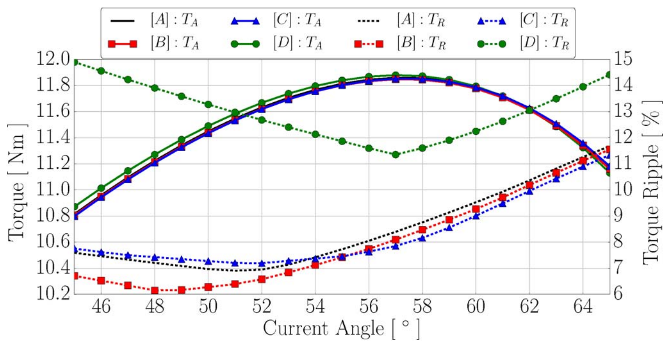

Fig. 10. Symmetric–asymmetric optimization objective torque ripple and average torque results versus current angle of the 24-slot machine, with [A]—$T_R(X_3)$, [B]—$T_R(X_5)$, [C]—$T_R(X_4)$, and [D]—$T_R(X_2)$.

TABLE III
SYMMETRIC–ASYMMETRIC OPTIMIZATION STRATEGY RESULTS OF THE 24-SLOT MACHINES

Step*	Stator Slots	Objective Function	θ [°]	T_A [Nm]	T_A [pu]	T_R [%]	T_R [pu]
Symmetric-Asymmetric Optimisation Strategy Results							
S_3	24	$T_R(X_2)$ - (Max T_A)	57	**11.88**	1.00	11.35	1.00
	24	$T_R(X_2)$ - (Min T_R)	57	11.88	1.00	**11.35**	1.00
S_4	24	$T_R(X_3)$ - (Max T_A)	57	**11.84**	1.00	7.85	0.69
	24	$T_R(X_3)$ - (Min T_R)	52	11.62	0.97	**7.19**	0.33
S_5	24	$T_R(X_4)$ - (Max T_A)	57	**11.86**	1.00	8.40	0.74
	24	$T_R(X_4)$ - (Min T_R)	51	11.54	0.98	**6.91**	0.61
S_6	24	$T_R(X_5)$ - (Max T_A)	57	**11.85**	1.00	8.10	0.71
	24	$T_R(X_5)$ - (Min T_R)	48	11.21	0.94	**6.15**	0.54

* - Simulation Step in Fig. 9 ; θ - Current Angle ; T_A - Average Torque ; T_R - Torque Ripple

objectives can be found in Table III. Here, the symmetric maximum T_A and minimum T_R current angle positions of objective S_3, for the 24-slot machine, are taken as the unity values for the per-unit value calculations.

From this table, the lowest achievable T_R is from S_6, with a 6% reduction in maximum T_A and a 46% reduction in T_R from the symmetric optimization. From this initial optimization study, the observation is made that a reduction in T_R is possible with the proposed flux barrier topology without affecting the T_A current angle mapping when implementing the proposed asymmetric flux barrier optimization. A further observation is that the maximum T_A point and minimum T_R point are not at the same current angle when implementing the specific asymmetric optimization strategy.

2) Full-Asymmetric Optimization Strategy: In an attempt to combine the reduction of T_R from $T_R(X_5)$ with the coherent current angle point for high T_A and low T_R from $T_R(X_2)$, a full-asymmetric optimization strategy is implemented. The strategy includes a $T_A(X_6)$ objective function with variables X_6, as in Table II, and with the model asymmetrically maximized from the start utilizing the MMFD algorithm.

In the initial optimization study, it is noted that the optimizer maximized variables S_{1P} and S_{2P} to their maximum allowable area, as illustrated in Fig. 12. In the second optimization study, these variables were therefore omitted from the optimization variables, with an initial maximum value. This then clearly illustrates the desired flux barrier tip that the optimizer continuously tended to, with a single illustration in Fig. 7(a).

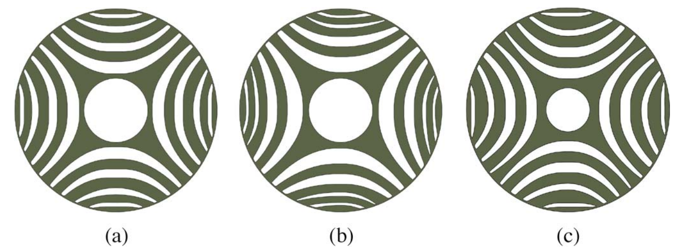

Fig. 11. Laminations of optimization objective results by objective functions. (a) $T_R(X_5)$ 24-slot machine lamination. (b) $T_R(X_8)$ 24-slot machine lamination. (c) $T_R(X_8)$ 36-slot machine lamination.

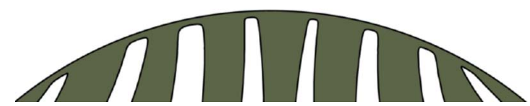

Fig. 12. Barrier tip illustration of optimization objective $T_R(X_8)$ of the 36-slot stator lamination in Fig. 11(c). This illustrates the ASPS and flattened barrier tips.

TABLE IV
FULL-ASYMMETRIC OPTIMIZATION STRATEGY VERSUS FULL-SYMMETRIC OPTIMIZATION STRATEGY RESULTS OF THE 24-SLOT AND 36-SLOT MACHINES

Sim*	Stator Slots	Objective Function	θ [°]	T_A [Nm]	T_A [pu]	T_R [%]	T_R [pu]
Full Symmetric Optimisation Strategy Results							
S_3	24	$T_R(X_2)$ - (Max T_A)	57	**11.88**	1.00	11.35	1.00
	24	$T_R(X_2)$ - (Min T_R)	57	11.88	1.00	**11.35**	1.00
S_3	36	$T_R(X_2)$ - (Max T_A)	66	**75.23**	1.00	8.49	1.00
	36	$T_R(X_2)$ - (Min T_R)	66	75.23	1.00	**8.49**	1.00
Full Asymmetric Optimisation Strategy Results							
A_1	24	$T_R(X_6)$ - (Max T_A)	52.2	**11.93**	1.00	51.54	4.54
	24	$T_R(X_6)$ - (Min T_R)	52.2	11.93	1.00	**51.54**	4.54
A_3	24	$T_R(X_8)$ - (Max T_A)	52.5	**11.83**	1.00	5.72	0.50
	24	$T_R(X_8)$ - (Min T_R)	52.5	11.83	1.00	**5.72**	0.50
A_1	36	$T_R(X_6)$ - (Max T_A)	64	**78.53**	1.04	52.79	6.22
	36	$T_R(X_6)$ - (Min T_R)	64	78.53	1.04	**52.79**	6.22
A_3	36	$T_R(X_8)$ - (Max T_A)	64	**77.06**	1.02	3.90	0.46
	36	$T_R(X_8)$ - (Min T_R)	64	77.06	1.02	**3.90**	0.46

* - Simulation Step in Fig. 9 ; θ - Current Angle ; T_A - Average Torque ; T_R - Torque Ripple

Once again, the two-step T_R minimization discussed in the initial optimization strategy is repeated, with variables X_7 in Table II allowed to vary asymmetrically for $T_R(X_7)$ minimization, implementing variables $X_6^{A_1}$ as start variables. This optimization is followed by $T_R(X_8)$ objective minimization, implementing the result variables $X_7^{A_2}$ from $T_R(X_7)$ as initial values. This optimization is conducted with θ constrained at the objective function $T_A(X_6)$ convergence point in order to force the optimizer to seek a mutual coherent maximum T_A and minimum T_R current angle point, as found with the symmetric optimization model $T_R(X_2)$.

The results of this strategy applied to both the 24-slot and 36-slot machines are tabulated in Table IV and illustrated in Fig. 14. In the table, the initial full-symmetric optimization $T_R(X_2)$ results of both stators are taken as unity for the per-unit calculations. Also shown in the table are the initial $T_A(X_6)$ maximization results, illustrating a slight drop in T_A during the two-step minimization of T_R.

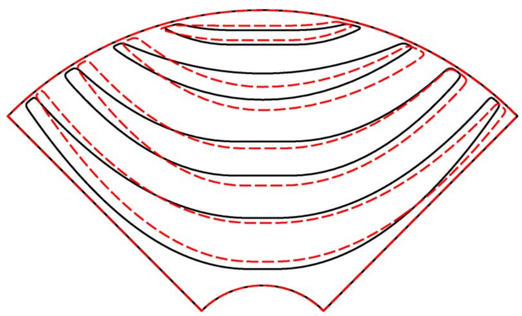

Fig. 13. Optimization result lamination of the (solid lines) full-symmetric and (dashed lines) full-asymmetric optimizations of the 36-slot stator illustrating the symmetric versus asymmetric pole structure.

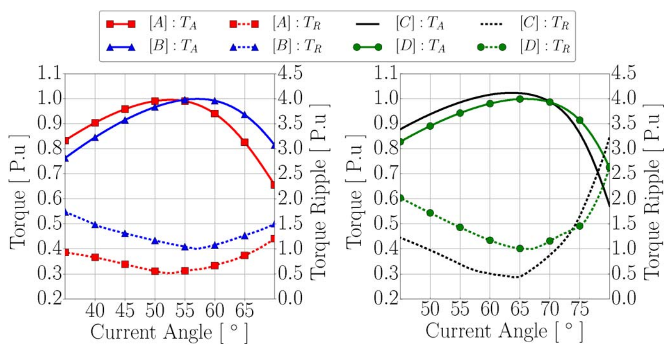

Fig. 14. Full-asymmetric optimization objective torque ripple and average torque results versus current angle comparison for the 24-slot and 36-slot machines with [A]—$T_R(X_2$ 24-slot machine, [B]—$T_R(X_8)$ 24-slot machine, [C]—$T_R(X_8)$ 36-slot machine, and [D]—$T_R(X_2)$ 36-slot machine.

From Fig. 14 and Table IV, it is evident that achieving a coherent maximum T_A and a minimum T_R point is possible with respect to the current angle. Furthermore, minimum torque ripple values of 3.9% and 5.7% are achieved for the 36-slot and 24-slot machines, respectively. Furthermore, a 2% increase in T_A is achieved for the 36-slot machine, compared to the full-symmetric and full-asymmetric optimization results of steps S_3 and A_3.

When comparing the first maximization of T_A, step A_1, to the final T_R minimization step A_3, the results of the 24-slot stator illustrate a 0.01% reduction in average torque, with a 88.9% reduction in T_R from 51.54% to 5.72%. Likewise, for the 36-slot stator, there was a 2% reduction in T_A, with a 92.6% reduction in T_R from 52.79% to 3.90%.

The optimized rotor flux barrier topology laminations of objective $T_R(X_5)$ and objective function $T_R(X_8)$ applied to the two 24-slot and 36-slot machines are illustrated in Fig. 11. A comparison between the full-symmetric $T_R(X_2)$ optimized lamination and full-asymmetric $T_R(X_8)$'s optimized lamination for the 36-slot stator is also shown in Fig. 13 to indicate the flux barrier variation.

IV. Effect of Rotor Skew on Proposed Topology

In this section, the effect of rotor skew on the five optimum topologies optimized is investigated. These topologies are as follows: $T_R(X_2)$ for the 24-slot and 36-slot machines and $T_R(X_5)$ of the 24-slot machine together with both the $T_R(X_8)$ objectives from the 24-slot and 36-slot machines. The process of investigation included a T_R contour mapping versus current

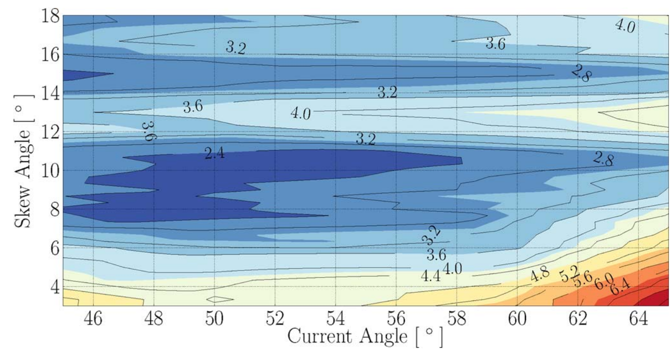

Fig. 15. Torque ripple versus skew and current angle mapping of the full-symmetric optimization objective function $T_R(X_2)$ of the 24-slot machine with one-slot pitch at 15.0°.

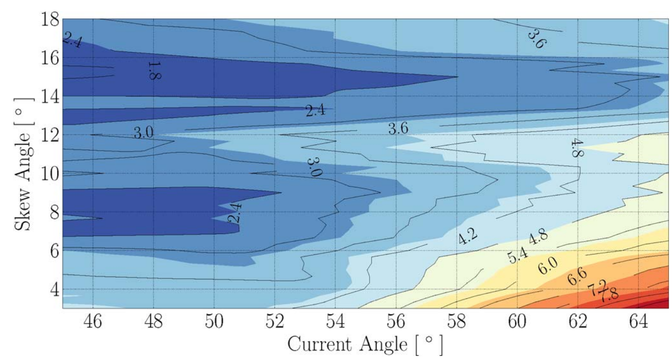

Fig. 16. Torque ripple versus skew and current angle mapping of the symmetric–asymmetric optimization objective function $T_R(X_5)$ of the 24-slot machine with one-slot pitch at 15.0°.

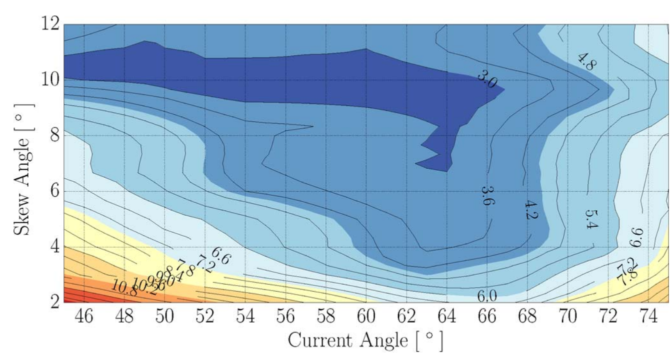

Fig. 17. Torque ripple versus skew and current angle mapping of the full-symmetric optimization objective function $T_R(X_2)$ of the 36-slot machine with one-slot pitch at 10.0°.

and skew angle. The average torque and torque ripple for each step of the mapping are calculated by dividing the machine into five respective machines, as described in [7].

The results of the T_R contour mapping for the initial SAS for the two implemented stator machines are presented in Figs. 15–17. The FAS T_R contour mapping results for the two machines in the second optimization strategy are illustrated in Figs. 19 and 20. In these figures, the traditional one-slot pitch skew for minimum torque ripple is clearly evident at the 15° area for the 24-slot machine and at the 10° area in the 36-slot machine. In addition, in the 24-slot machine mappings, a second low T_R area in the 7°–11° skew range is identified in all three 24-slot machine mapping figures, with an additional low

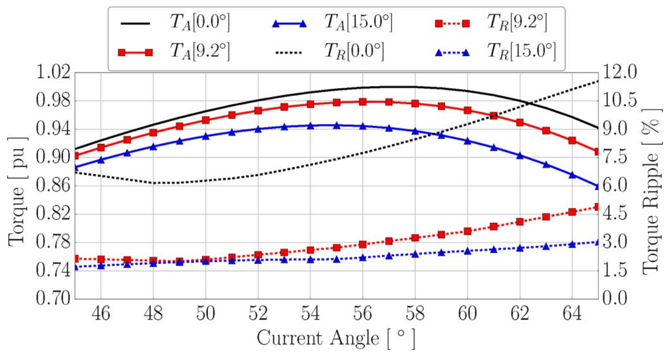

Fig. 18. Symmetric–asymmetric optimization objective function $T_R(X_5)$ average torque and torque ripple versus current angle for the selected skew angles 0.0°, 9.2°, and 15.0° for the 24-slot machine.

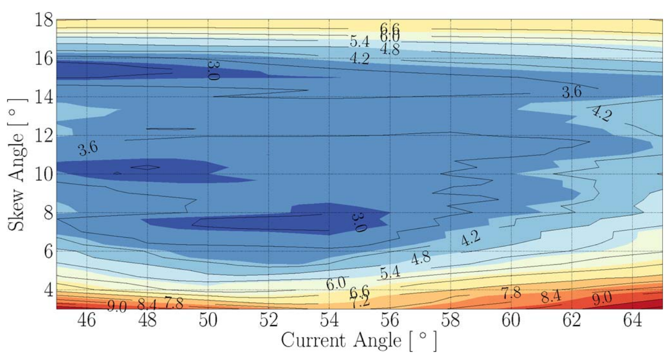

Fig. 19. Torque ripple versus skew and current angle mapping of the full-asymmetric optimization objective function $T_R(X_8)$ of the 24-slot machine with #tone-slot pitch at 15.0°.

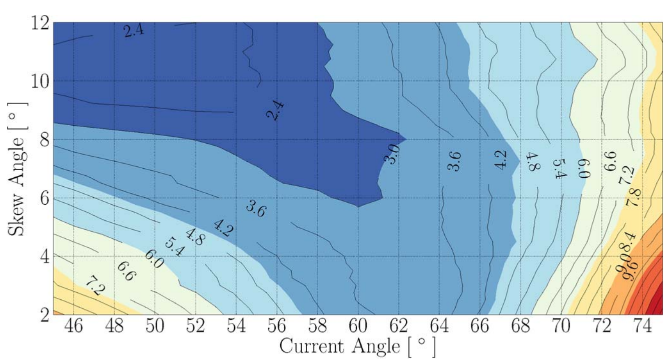

Fig. 20. Torque ripple versus skew and current angle mapping of the full-asymmetric optimization objective function $T_R(X_8)$ of the 36-slot machine with one-slot pitch at 10.0°.

torque ripple area in the 4°–10° skew range for the 36-slot machine mappings.

For the investigation of the 36-slot mapping, two additional angles, namely, 3.0° or 4.0° and 8.0°, are selected along with the one-slot pitch angle and unskewed machine. For the 24-slot machine, one additional angle per topology is selected, which includes a 10.6° skew angle for the mapping in Fig. 15, a 9.2° skew angle for the mapping in Fig. 16, and a 7.6° skew angle for Fig. 19. The results of this investigation are tabulated in Tables V and VI, with the 0.0° skew results taken as the unity value for the per-unit calculation values for each machine analyzed. Comparative current angle maps for the investigated machines from the symmetric–asymmetric optimization strategy objective $T_R(X_5)$ and full-asymmetric optimization objective

TABLE V
SKEW ANGLE RESULTS OF THE TWO APPLIED OPTIMIZATION STRATEGY TOPOLOGIES

Skew Angle Mapping						
Stator Slots	Skew Angle	θ [°]	T_A [Nm]	T_A [pu]	T_R [%]	T_R [pu]
Symmetric-Asymmetric Strategy						
Step S_3 - $T_R(X_2)$						
Figure 15 Result Analysis						
24	**0.0°** - (Max T_A)	57	**11.88**	1.00	11.35	1.00
24	**0.0°** - (Min T_R)	57	11.88	1.00	**11.35**	1.00
24	**10.6°** - (Max T_A)	53	**11.50**	0.97	2.14	0.19
24	**10.6°** - (Min T_R)	53	11.47	0.97	**2.1**	0.19
24	**15.0°** - (Max T_A)	50	**11.19**	0.94	2.6	0.23
24	**15.0°** - (Min T_R)	45	11.0	0.93	**2.28**	0.20
Step S_6 - $T_R(X_5)$						
Figure 16 Result Analysis						
24	**0.0°** - (Max T_A)	57	**11.85**	1.00	8.10	1.32
24	**0.0°** - (Min T_R)	48	11.21	0.95	**6.15**	1.00
24	**9.2°** - (Max T_A)	56	**11.59**	0.98	2.90	0.47
24	**9.2°** - (Min T_R)	49	11.18	0.94	**2.01**	0.33
24	**15.0°** - (Max T_A)	55	**11.20**	0.95	2.12	0.35
24	**15.0°** - (Min T_R)	45	10.50	0.89	**1.72**	0.28
Step S_3 - $T_R(X_2)$						
Figure 17 Result Analysis						
36	**0.0°** - (Max T_A)	66	**75.23**	1.00	8.97	1.00
36	**0.0°** - (Min T_R)	66	75.23	1.00	**8.97**	1.00
36	**4.0°** - (Max T_A)	66	**74.98**	1.00	3.83	0.43
36	**4.0°** - (Min T_R)	66	74.66	1.00	**2.87**	0.32
36	**8.0°** - (Max T_A)	65	**74.22**	0.99	3.15	0.35
36	**8.0°** - (Min T_R)	53	74.19	0.99	**2.87**	0.32
36	**10.0°** - (Max T_A)	64	**73.66**	0.98	2.66	0.30
36	**10.0°** - (Min T_R)	63	73.58	0.98	**2.53**	0.28

θ - Current Angle ; T_A - Average Torque ; T_R - Torque Ripple

TABLE VI
SKEW ANGLE RESULTS OF THE TWO APPLIED OPTIMIZATION STRATEGY TOPOLOGIES

Skew Angle Mapping						
Stator Slots	Skew Angle	θ [°]	T_A [Nm]	T_A [pu]	T_R [%]	T_R [pu]
Full Asymmetric Strategy						
Step A_3 - $T_R(X_8)$						
Figure 19 Result Analysis						
24	**0.0°** - (Max T_A)	53	**11.83**	1.00	5.72	1.00
24	**0.0°** - (Min T_R)	53	11.83	1.00	**5.72**	1.00
24	**7.6°** - (Max T_A)	56	**11.66**	0.99	3.28	0.57
24	**7.6°** - (Min T_R)	54	11.62	0.99	**2.84**	0.50
24	**15.0°** - (Max T_A)	49	**11.18**	0.95	2.58	0.45
24	**15.0°** - (Min T_R)	45	10.99	0.93	**2.27**	0.40
Step A_3 - $T_R(X_8)$						
Figure 20 Result Analysis						
36	**0.0°** - (Max T_A)	64	**77.06**	1.00	3.90	1.00
36	**0.0°** - (Min T_R)	64	77.06	1.00	**3.90**	1.00
36	**3.0°** - (Max T_A)	63	**76.92**	1.00	3.19	0.82
36	**3.0°** - (Min T_R)	63	76.92	1.00	**3.19**	0.82
36	**8.0°** - (Max T_A)	63	**76.05**	0.98	3.12	0.80
36	**8.0°** - (Min T_R)	56	74.23	0.96	**2.68**	0.69
36	**10.0°** - (Max T_A)	62	**75.49**	0.97	3.56	0.91
36	**10.0°** - (Min T_R)	49	69.24	0.90	**1.83**	0.47

θ - Current Angle ; T_A - Average Torque ; T_R - Torque Ripple

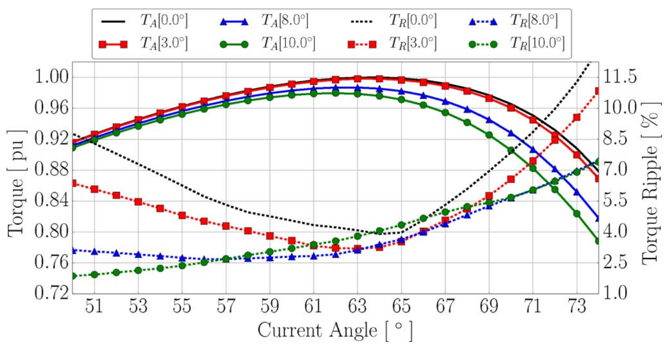

Fig. 21. Full-asymmetric optimization objective function $T_R(X_8)$ average torque and torque ripple versus current angle for the selected skew angles 0.0°, 3.0°, 8.0°, and 10.0° for the 36-slot machine.

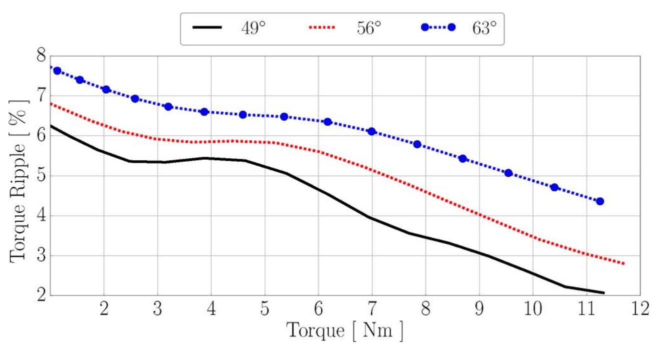

Fig. 22. Average torque versus torque ripple of the selected $T_R(X_5)$ optimization objective machine with constant current angles at 49°, 56°, and 63°.

$T_R(X_8)$ for the 36-slot and 24-slot machines with selected skew angles are indicated in Figs. 18 and 21.

From the results in Tables V and VI, it is evident that, although the lowest possible T_R is achieved with the traditional one-slot pitch skew in most cases, this angle is not the optimum if T_A is also taken into account. The variation of T_R and T_A with skew angle and current angle is clearly visible in Figs. 18 and 21. This variation is more pronounced for the 24-slot machine due to its larger one-slot pitch skew angle.

Considering the two T_R mappings of the 24-slot machine for the two different topologies found by $T_R(X_5)$ and $T_R(X_8)$ in Figs. 16 and 19, it is clear that the effective angle for rotor skew heavily depends on the specific rotor topology. Furthermore, an interesting trend is observed with the 24-slot machine, where the three mappings have low T_R values in the 60°–70° slot pitch angle areas. These angles provide improved machine performance parameters compared to the conventional one-slot pitch skew.

V. Machine Manufacture and Testing

In order to verify the optimized topologies, objective function $T_R(X_5)$'s optimized rotor is selected for manufacturing. This includes the 9.2° skew angle, which is perceived to be the optimum skew angle for the objective topology as in Table V. The respective average torque versus torque ripple plot for three constant current angles is illustrated in Fig. 22. In addition, the torque versus electrical angle from rotor skew angles 0°, 9.2°, and 15° is illustrated in Fig. 23 for the selected rotor.

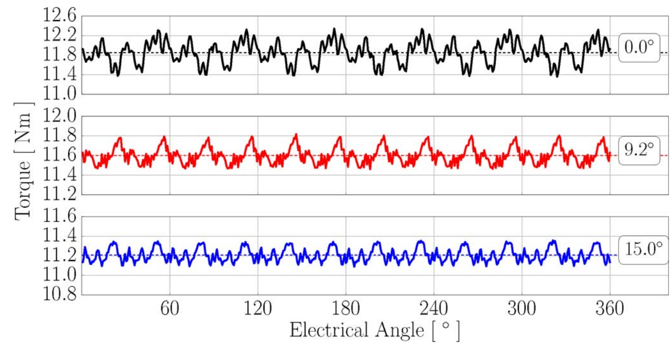

Fig. 23. Torque waveforms for the selected 24-slot machine for manufacture that include the 0°, 9.2°, and 15° skew angles.

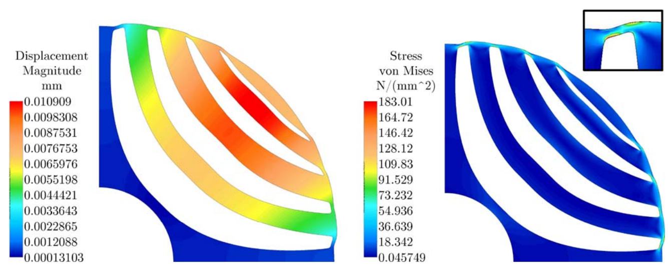

Fig. 24. Stress and deformation contour plot of the selected $T_R(X_5)$ lamination at 6000 r/min with only centrifugal forces applied.

TABLE VII
Stress and Deformation Analysis and Comparison Between Structural Analysis Done in JMag and Algor Multiphysics on the Selected Rotor Lamination

Stress & Deformation Analysis						
			JMag		*Algor*	
Speed [pu]	Temp♣ [C°]	E-M♠	Mises ℜ [MPa]	Def * [μm]	Mises ℜ [MPa]	Def * [μm]
4	20	NA	172	10.5	183	10.9
4	20	√	207	12.4	NA	NA
4	150	NA	172	69.4	183	69.6
4	150	√	207	71.3	NA	NA

Lamination M470-50A Yield Strength : 300 MPa
♣ - Lamination Temperature ; ♠ - Electromagnetic Forces
ℜ - Von Mises Peak Stress ; * - Maximum Point Deformation

Due to the omission of the central support web in the lamination, an extensive structural analysis was conducted to verify the structural integrity of the lamination at rated conditions. An illustration of the stress and deformation analysis contour plot is provided in Fig. 24, with the tabulated results in Table VII. The rotor lamination was simulated at four times the rated machine speed (i.e., 6000 r/min), with lamination temperatures varying between a minimum of 20 °C and a maximum of 150 °C. Simulation results include the simulation of the lamination by only including centrifugal forces and, second, by including centrifugal and rated condition electromagnetic forces, with the largest contributor to stress and deformation being the centrifugal forces.

In order to verify the initial structural simulation done in JMAG, the comparative structural analysis was repeated in Algor Multiphysics, with a comparison made in Table VII that

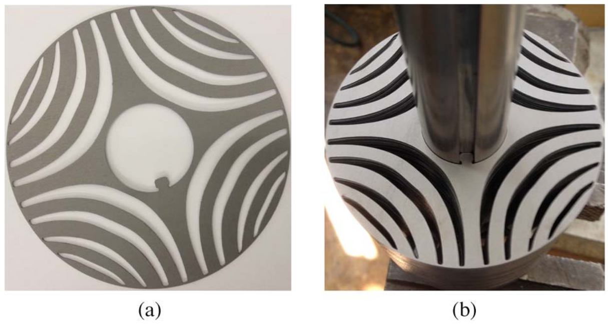

Fig. 25. Illustration of $T_R(X_5)$ lamination and rotor assembly. (a) $T_R(X_5)$ lamination. (b) $T_R(X_5)$ rotor assembly.

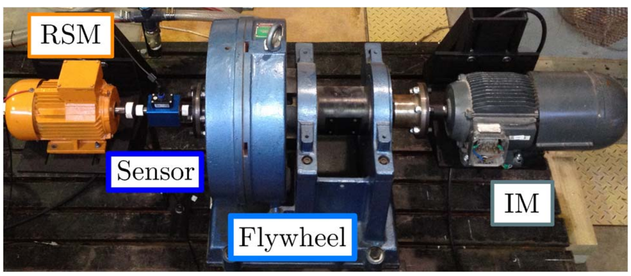

Fig. 26. Back-to-back RSM IM test bench setup with flywheel for IM torque harmonic filter.

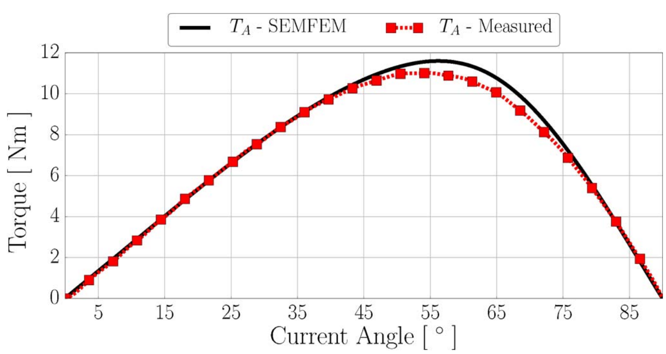

Fig. 27. Measured T_A results plotted against the FE simulation of the manufactured 9.2°, objective function $T_R(X_5)$ machine.

excludes the electromagnetic forces at rated conditions. This is due to the inability of Algor to accurately include rated condition electromagnetic forces. Taking the yield strength of the lamination material into account, the peak stress and deformation of the lamination is found to be well within acceptable levels, thus proving rotor structural integrity at rated operating conditions. The manufactured rotor lamination is illustrated in Fig. 25(a), with the rotor assembly shown in Fig. 25(b). The test bench setup is illustrated in Fig. 26.

The measured results of the manufactured rotor machine are indicated in Figs. 27 and 28. The measured T_A values of Fig. 27 closely correlate with the simulated values across the current angle range, with a maximum deviation of 5%. The latter deviation can be attributed to the difference in the stator steel characteristics used in the FE package. Additionally, the actual induction machine, a from-the-shelf induction machine stator whose exact flux density and magnetic field strength characteristics curve characteristics were not known to the authors, was used in the experiments.

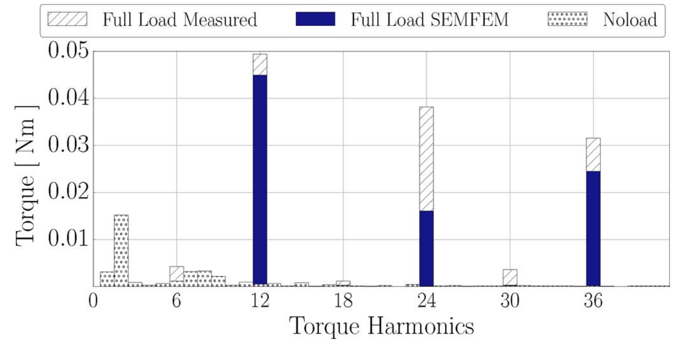

Fig. 28. Torque ripple harmonic plot of the measured torque, with rated conditions at 20 r/min. "Noise" harmonics from the test bench at no load conditions are also illustrated.

The torque ripple harmonic comparison in Fig. 28 also illustrates, in general, a good comparison between measured and simulated results. The only exception is the large difference in the measured and the simulated 24th harmonic torque component. This is difficult to explain, as it could be due to inaccuracies in the rotor manufacturing, differences in the dimensions of the FE package stator, and the actual-induction-machine stator and/or inaccuracy in the exact skew angle of the rotor. The latter statement is motivated by the extreme sensitivity of torque ripple in the selected 9.2° skew angle range as illustrated in Fig. 16.

VI. Conclusion

In this paper, an alternative asymmetric flux barrier creation technique is proposed in combination with design optimization to maximize average torque and minimize torque ripple. It is shown that, by implementing a relatively high number of variables of between 29 and 37, torque ripple values of 5.7% and 3.9% are achievable for the 24-slot and 36-slot machine stators, respectively, without implementing rotor skew. Moreover, it is shown that there is no drop in T_A when comparing the full-symmetric with the full-asymmetric optimizations, with an average torque ripple reduction of 50% for the 24-slot and 36-slot machines, respectively. This large reduction in torque ripple with the proposed asymmetric topology is confirmed by a similar study conducted in [20]. Additionally, the optimum flux barrier tip found for the optimized topology was flattened and not rounded (see Fig. 12).

It is further shown that a torque ripple of below 3.0% is achievable by implementing rotor skew for both 24-slot and 36-slot machines. This is achieved with rotor skew angles of between 60% and 70% of a slot pitch angle for the 24-slot machine and between 30% and 80% for a 36-slot machine. The rotor skew analysis illustrates that the optimum rotor skew angle heavily depends not only on the specific stator configuration but also on the rotor topology.

Rotor integrity was proven to be well within the limit at rated operating conditions. The average torque comparison between simulated and measured results correlates closely with the torque ripple harmonic comparison between the measured and simulated values also correlating well with a slight increase in measured harmonics.

References

[1] A. Vagati *et al.*, “Improvement of synchronous reluctance motor design through finite-element analysis,” in *Conf. Rec. 34th IEEE IAS Annu. Meeting*, 1999, pp. 862–871.

[2] M. Kamper, F. Van der Merwe, and S. Williamson, “Direct finite element design optimisation of the cageless reluctance synchronous machine,” *IEEE Trans. Energy Convers.*, vol. 11, no. 3, pp. 547–555, Sep. 1996.

[3] R.-R. Moghaddam, F. Magnussen, and C. Sadarangani, “Novel rotor design optimization of synchronous reluctance machine for low torque ripple,” in *Proc. 20th Int. Conf. Elect. Mach.*, Sep. 2012, pp. 720–724.

[4] G. Pellegrino, F. Cupertino, and C. Gerada, “Barriers shapes and minimum set of rotor parameters in the automated design of synchronous reluctance machines,” in *Proc. IEEE IEMDC*, 2013, pp. 1204–1210.

[5] F. Cupertino, B. Dei, and C. Gerada, “Design of synchronous reluctance machines with multi-objective optimization algorithms,” in *Proc. IEEE IEMDC*, 2013, pp. 1858–1865.

[6] M. J. Kamper and W. T. Villet, “Design and performance of compensated reluctance synchronous machine drive with extended constant power speed range,” in *Proc. IEEE ECCE*, Sep. 2012, pp. 4330–4337.

[7] X. Bomela and M. Kamper, “Effect of machine design on performance of reluctance synchronous machine,” in *Conf. Rec. IEEE IAS Annu. Meeting*, 2000, vol. 1, pp. 515–522.

[8] M. H. A. Prins, C. W. Vorster, and M. J. Kamper, “Reluctance synchronous and field intensified-PM motors for variable-gear electric vehicle drives,” in *Proc. IEEE Energy Convers. Congr. Expo.*, Sep. 2013, pp. 657–664.

[9] W. T. Villet, M. H. A. Prins, C. W. Vorster, and M. J. Kamper, “Saliency performance investigation of synchronous machines for position sensorless controlled EV drives,” in *Proc. SLED/PRECEDE*, 2013, pp. 1–8.

[10] P. Alotto, M. Barcaro, N. Bianchi, and M. Guarnieri, “Optimization of IPM motors with Machaon rotor flux barriers,” in *Proc. 14th Biennial IEEE CEFC*, 2010, p. 1.

[11] M. Ferrari, N. Bianchi, A. Doria, and E. Fornasiero, “Design of synchronous reluctance motor for hybrid electric vehicles,” in *Proc. Int. Elect. Mach. Drives Conf.*, May 2013, pp. 1058–1065.

[12] N. Bianchi, M. Degano, and E. Fornasiero, “Sensitivity analysis of torque ripple reduction of synchronous reluctance and interior PM motors,” in *Proc. IEEE ECCE*, 2013, pp. 1842–1849.

[13] M. Ferrari, N. Bianchi, and E. Fornasiero, “Rotor saturation impact in synchronous reluctance and PM assisted reluctance motors,” in *Proc. IEEE Energy Convers. Congr. Expo.*, Sep. 2013, pp. 1235–1242.

[14] A. Fratta, G. Troglia, A. Vagati, and F. Villata, “Evaluation of torque ripple in high performance synchronous reluctance machines,” in *Conf. Rec. 28th IEEE IAS Annu. Meeting*, 1993, pp. 163–170.

[15] A. Vagati, M. Pastorelli, G. Franceschini, and C. Petrache, “Design of low-torque-ripple synchronous reluctance motors,” *IEEE Trans. Ind. Appl.*, vol. 34, no. 4, pp. 758–765, Jul./Aug. 1998.

[16] G. N. Vanderplaats, *Algorithms and Theory of Computation Handbook*, 1st ed. Boca Raton, FL, USA: CRC Press, 1999. pp 1715–1717.

[17] S. Gerber, “A finite element based optimisation tool for electrical machines,” M.Sc. thesis, Dept. Elect. Electron. Eng., Univ. Stellenbosch, Stellenbosch, South Africa, 2011. [Online]. Available: http://hdl.handle.net/10019.1/6635

[18] *VisualDOC User Manual*, version 6.0 ed., Vanderplaats Research & Development Inc., Colorado Springs, CO, USA.

[19] G. N. Vanderplaats, *Multidiscipline Design Optimisation*, vol. First Edition. Colorado Springs, CO, USA: Vanderplaats Research & Development, Inc., 2007, pp. 224–234, 194–197.

[20] T. Lange, B. Kerdsup, C. Weiss, and R. De Doncker, “Torque ripple reduction in reluctance synchronous machines using an asymmetric rotor structure,” in *Proc. 7th IET Int. Conf. PEMD*, Apr. 2014, pp. 1–5.

Eduan Howard (S’14) received the B.Eng. degree in mechanical engineering from the University of Stellenbosch, Stellenbosch, South Africa, in 2012, where he is currently working toward the M.Sc. (Eng.) degree in the Department of Electrical and Electronic Engineering.

His current research focus is on reluctance synchronous machines for wind turbine purposes and includes the optimizing of reluctance synchronous machine technologies, including computer-aided design.

Maarten J. Kamper (SM’08) received the M.Sc. (Eng.) and Ph.D. (Eng.) degrees from the University of Stellenbosch, Stellenbosch, South Africa, in 1987 and 1996, respectively.

Since 1989, he has been with the Department of Electrical and Electronic Engineering, University of Stellenbosch, where he is currently a Professor of electrical machines and drives. His research interests include the design optimization and control of electrical machines, currently with the focus on wind generators and industrial and electric vehicle drives.

Prof. Kamper is an Associate Editor of the Electric Machines Committee of the IEEE TRANSACTIONS ON INDUSTRY APPLICATIONS. He also serves on the Steering Committee of the International Conference on Electrical Machines.

Stiaan Gerber (S’13) was born in Bellville, South Africa, on February 20, 1986. He received the B.Eng. degree (*cum laude*) in the field of electrical and electronic engineering with computer science and the M.Sc.Eng. degree (*cum laude*) from the University of Stellenbosch, Stellenbosch, Africa, in 2008 and 2011, respectively, where he is currently working toward the Ph.D. degree in the field of electrical machines, with specific focus on magnetically geared electrical machines.

His main research interests in the engineering field are electrical machine design, numerical optimization, renewable energy power generation, and finite-element methods.